Metallomics

COMMUNICATION

View Article Online
View Journal | View Issue

Check for updates

Cite this: *Metallomics*, 2019, **11**, 1344

Received 24th May 2019,
Accepted 18th July 2019

DOI: 10.1039/c9mt00134d

rsc.li/metallomics

Published on 18 July 2019. Downloaded by Nottingham Trent University on 8/18/2019 11:29:11 AM.

Imaging and proteomic study of a clickable iridium complex†

Xiuxiu Wang,[a] Jingyi Zhang,[b] Xinyang Zhao,[b] Wei Wei *[a] and Jing Zhao *[b]

Iridium complexes have recently attracted increasing interest in developing metallodrugs. Herein, we have synthesized and characterized a clickable iridium hydride complex 2-N3. The cytotoxity and production of reactive oxygen species study in A2780 cancer cells indicated a potent anticancer activity of 2-N3. The ICP-MS analysis and the cellular imaging *via* Cu(I) catalyzed azide–alkyne cycloaddition suggested the accumulation of 2-N3 in the nucleus and cytoplasm. Further label-free quantitative proteomic analysis indicated that the ECM–receptor interaction pathway was activated by 2-N3. The analysis of down-regulated proteins suggested that 2-N3 affected cellular DNA transcription, post-translational glycosyl modification, and redox homeostasis. Besides, 2-N3 also damaged several crucial proteins and enzymes in the mitochondria and nucleus, leading to the disorder of the cellular processes. Our results provide a new approach to mechanism studies of metallodrugs combining click chemistry and proteomic analysis.

Significance to metallomics

Recently, considerable progress has been made in the development of metallodrugs. However, mechanism of action studies are a long standing challenge due to their diverse interactions with different biomacromolecules. Herein we developed a clickable anticancer iridium complex **2-N3**, which can be imaged in cells *via* cellular click reaction. Furthermore, proteomic analysis is of crucial importance for mechanistic understanding. Through label-free quantitative proteomics analysis, we found that pathways for expression of several crucial proteins and enzymes and their related cell processes were significantly decreased or damaged by Ir(III) complex **2-N3**. Our results provide a new approach to mechanism studies of metallodrugs combining click chemistry and proteomic analysis.

Introduction

Considerable progress has been made in the design and synthesis of anticancer metallodrugs including platinum, ruthenium and iridium complexes.[1–3] Organoiridium complexes were selected for their inert coordinative bonds and stable scaffolds.[4,5] Iridium(III) complexes were reported as potential anticancer agents bearing various functional ligands with novel mechanisms, including mitochondrial dysfunction,[6] reactive oxygen species (ROS) production[3] and inhibition of tumor necrosis factors.[7] Recently, bidentate arylnitrone ligands (PBN), considered as an effective radical scavenger,[8] have been demonstrated to prevent neuroinflammation and possess potent anticancer activity.[9–11] Cancer cells are constantly under high oxidative stress, and change of intracellular ROS levels may significantly affect their proliferation. This observation implies that cancer cells might be preferentially eliminated by pharmacologically generated ROS.[12] The combination of organoiridium with PBN showed excellent catalytic anticancer activity in HepG2 human liver cancer cells, with an IC_{50} value about 26-fold lower than that of the clinical drug cisplatin.[13]

Imaging study on the process of small molecule trafficking in cells is an intuitive and visible approach for mechanism of action studies, especially for metal-based anticancer agents. The well-known clinical platinum drugs such as cisplatin or carboplatin,[14] are generally considered to be absorbed passively, forming exchange-inert complexes with genomic DNA.[15,16] Bierbach and co-workers imaged DNA-targeted platinum drugs in cancer cells by confocal fluorescence microscopy *via* click reaction of an azide functionalized platinum–acridine complex with the alkyne dye Alexa Fluor 488, which showed that the platinum acridine reagent primarily accumulated in the nucleus of NCI–H460 cancer cells.[17] Recently, a report on the post-treatment modification of Pt(II) complexes by DeRose *et al.* showed intense nuclear localization using the bioorthogonal

[a] *State Key Laboratory of Coordination Chemistry, Institute of Chemistry and Biomedical Sciences, School of Life Sciences, Nanjing University, Nanjing 210023, China. E-mail: weiwei@nju.edu.cn*

[b] *School of Chemistry and Chemical Engineering, Nanjing University, Nanjing 210023, China. E-mail: jingzhao@nju.edu.cn*

† Electronic supplementary information (ESI) available: Experimental procedures and characterization data for all new compounds. CCDC 1514789. For ESI and crystallographic data in CIF or other electronic format see DOI: 10.1039/c9mt00134d

This journal is © The Royal Society of Chemistry 2019

Published on 18 July 2019. Downloaded by Nottingham Trent University on 8/18/2019 11:29:11 AM.

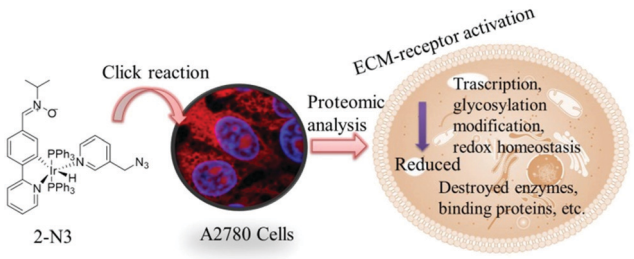

Fig. 1 Summary of click reaction-enabled cellular imaging and proteomic analysis of iridium hydride complex **2-N3**.

Cu(I) catalyzed azide–alkyne cycloaddition (CuAAC) reaction in cells.[18] Metal terpenoids by Lo *et al.* were another representative intracellular imaging of iridium(III) complexes in cells, as Ir(III) was modified with a nitrone unit to perform a bioorthogonal reaction intracellularly.[19] Therefore, post-treatment of the Ir complex with azide modification, which can react with alkyne-fluorophores *via* the Cu(I) catalyst later, seems to be a promising approach in studying the mechanism and target location of iridium metallodrugs.

In the current work, we designed, synthesized and characterized an iridium hydride complex incorporating both an azide group and a nitrone ligand. Based on previous work,[13] we kept the nitrone group free in PBN ligand. The cytotoxity and detection of ROS of **2-N3** in A2780 cancer cells were determined. The cellular imaging was studied by fluorescence microscopy *via* CuAAC reaction, and the proteomic analysis of **2-N3** treated cells was investigated (Fig. 1).

Results and discussion

Cytotoxity assay of 2-N3

Firstly, we synthesized the iridium hydride complex **2-N3** with free nitrone ligand and AMP ligand *via* C–H activation; the synthetic route was summarized in Scheme S1 (ESI†). Crystal of **2-N3** suitable for X-ray diffraction analysis was also obtained (Fig. 2a). Then the anticancer activity of **2-N3** was determined toward various cancer cell lines and one healthy cell line. Cytotoxicity research indicated that **2-N3** exhibited powerful anticancer activity towards A2780 human ovarian cancer cells with an IC_{50} value of 0.98 μM, while the nitrone ligand and AMP ligand displayed no significant anti-proliferative activity toward cancer cells, indicating that the combination of iridium and nitrone ligand and AMP ligand was essential for anti-proliferation (Table 1).

Mechanistic investigation

To explore the anticancer mechanism of **2-N3**, the cellular uptake and distribution of **2-N3** were studied first. After the extraction of **2-N3** treated cell components including the nucleus, mitochondria and cytosome, the iridium content was detected by ICP-MS. The results indicated that **2-N3** was mainly accumulated in the mitochondria (49.8%), cytoplasm (31.7%), and nucleus (18.5%, Fig. 2b). The nucleus accumulation indicated that **2-N3**

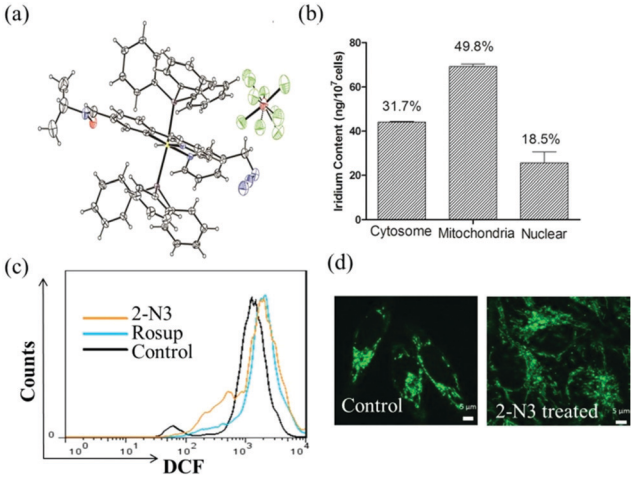

Fig. 2 (a) X-ray crystal structure of complex **2-N3** with thermal ellipsoids drawn at 50% probability. The hydrogen atoms and counter ions have been omitted for clarity. (b) Cellular distribution of iridium contents in A2780 cells after dealing with complex **2-N3** at 37 °C incubation for 3 h. (c) ROS production in A2780 cancer cells treated with complex **2-N3** for 3 h by flow cytometry detection, Rosup as positive control and non-treated cells as a negative control. (d) Morphological change of mitochondria in **2-N3** treated cells (37 °C, 3 h) compared with non-treated cells. Mitochondria were stained by Mito Track Green (MTG). Fluorescence channel: excitation wavelength, 490 nm; emission collected, 512 nm. Scale bar: 5 μm.

was able to penetrate the nuclear membrane. As **2-N3** showed the highest content in mitochondria, fluorescence microscope imaging of mitochondria was determined which displayed mitochondrial destruction in **2-N3** treated cells (Fig. 2d). Destruction of mitochondria is often related to an imbalance of intracellular redox levels, build-up of ROS, and an altered redox status in cancer cells.[12] Both fluorescence detection and flow cytometry detection indicated that the over–production of ROS induced by **2-N3** might be one of the main causes for its potent anticancer activity (Fig. 2c and Fig. S1, ESI†).

Imaging of 2-N3 in cells

To further identify the cellular location of **2-N3**, a click reaction-enabled imaging of **2-N3** in A2780 cancer cells was conducted based on a recently reported CuAAC click reaction of post-treatment of Pt(II) complexes in cells.[18] The click reaction required an alkyne fluorophore that was based on the common fluorochrome rhodamine. Encouraged by its apparent enhanced activity, we pursued cellular localization studies using fluorescence microscopy by treating A2780 cells with 3 μM **2-N3** and labelling with alkyne-containing rhodamine fluorophore under CuAAC catalytic conditions. Ir(III) complexes with fluorophore probes were scattered in the mitochondria, nucleus and cytoplasm (Fig. 3b), presenting multiple targets in cancer cells in a visible way. Importantly, the Cu-free controls displayed no fluorescence from nonspecific fluorophore interactions. These promising imaging results displayed the promise of complex **2-N3** for further localization studies by click chemistry.

Proteomic analysis of 2-N3 treated A2780 cells

Proteins, such as kinases and coenzymes, have become the main targets of metal complexes.[20] Meggers *et al.* reported that

Published on 18 July 2019. Downloaded by Nottingham Trent University on 8/18/2019 11:29:11 AM.

Table 1 IC_{50} value of complex **2-N3** and ligands, compared with cisplatin in different cancer cell lines A549, A2780, MCF-7, HepG-2 and H1299 and healthy cell line L-02

IC50 (μM)	A549	A2780	MCF-7	HepG-2	H1299	L-02
2-N3	1.44 ± 0.35	0.98 ± 0.05	4.46 ± 1.96	4.51 ± 0.66	5.28 ± 1.62	5.87 ± 0.41
AMP ligand	>50	>50	>50	>50	>50	>50
Nitrone ligand	>50	>50	>50	>50	>50	>50
Cisplatin	22.13 ± 2.22	17.08 ± 3.23	17.24 ± 5.28	27.71 ± 2.31	40.58 ± 0.51	>50

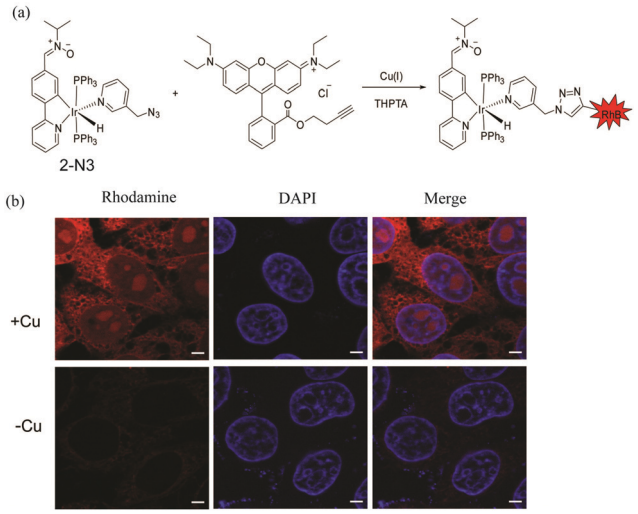

Fig. 3 Imaging of complex **2-N3** in A2780 cells *via* CuAAC click reaction. (a) CuAAC reaction of **2-N3** and alkyne-containing rhodamine RhB–alkyne. (b) Image of complex **2-N3** localization in HeLa cells. The Cu-free control and the alkyne-containing rhodamine fluorophore show no fluorescence in the nucleus. The red rhodamine fluorescence channel: excitation wavelength, 558 nm; emission collected, 575 nm. The blue Hoechst fluorescence channel: excitation wavelength, 353 nm; emission collected, 465 nm scale bar: 5 μm.

ruthenium and iridium complexes were found to be PIM2 kinase and TNF-α inhibitors.[21,22] Recently, proteomics-based studies by Keppler *et al.* have provided an excellent approach to unveil the modes of action of ruthenium(arene) complexes.[23,24] In the latest report, label-free quantitative proteomics revealed NNMT as a master metabolic regulator of cancer-associated fibroblasts.[25] To further explore the anticancer mechanism, we conducted label-free quantitative proteomics profiling. After proteomic analysis, we found that the expression levels of 18 proteins were significantly increased in **2-N3**-treated cells, while 8 proteins decreased (Fig. 4a and b).

Firstly, these different proteins were classified and analyzed with Blast2GO for gene ontology (GO) annotation.[26] The GO database classifies functions in organisms into three categories: the involved biological process (BP), the molecular function (MF), and the cell component (CC). The results of Level 2 analysis showed that the differentially expressed proteins were mainly involved in cellular biological metabolic processes, binding proteins and the cell part (Fig. 4c).

In bioorganisms, pathway analysis is the most direct and necessary way to identify the biological processes of cells and the mechanisms of action. To further understand the metabolic or signalling pathways that drugs may be involved in, the KEGG (Kyoto Encyclopedia of Genes and Genomes) pathway database, which contains information on metabolism, genetic information processing, cellular processes, human diseases and drug development, is commonly used for pathway screening research.[27] By annotating the KEGG pathway for the 26 proteins that are significantly differentially expressed in **2-N3** treated cells, we found that the pathways including amoebiasis disease related pathway, ECM–receptor interaction, cancer, toxoplasmosis, vitamin digestion and absorption and pyrimidine metabolism pathways were affected by **2-N3** (Fig. 4d). In both amoebiasis and ECM–receptor pathways, expression of laminin proteins LAMC1 and LAMB2 increased, indicating ECM–receptor activation by **2-N3**.

As described, the decreased proteins by **2-N3** included GAPDH, ubiquitin-like modifier-activating enzyme 5 (UBA5), dolichol-phosphate mannosyltransferase subunit 3 (DPM3), zinc finger ran-binding domain-containing protein 2 (ZRANB2), phosphatidylinositol-binding clathrin assembly protein (PICALM), mitochondrial 28S ribosomal protein S14 (MRPS14), sulfhydryl oxidase 2 (QSOX2) and proteasome subunit beta. Among these proteins, the most significant decline was DPM3 (71.93%), which is a stabilizer subunit of the dolichol-phosphate mannose (DPM) synthase complex and involved in the pathway of protein glycosylation, a type of protein modification.[28] Inhibition of DPM3 by **2-N3** probably affected the glycosylation process of proteins. The zinc finger ran-binding domain-containing protein 2 (decreased *ca.* 65%) was a splice factor required for alternative splicing of TRA2B/SFRS10 transcripts and may interfere with constitutive 5′-splice site selection.[29] The inhibition of ZRANB2 by **2-N3** may affect the mRNA transcription process. Besides, the down-regulation of sulfhydryl oxidase 2 (*ca.* 51%), which catalyzes the oxidation of sulfhydryl groups in peptide and protein thiols to disulfides with the reduction of oxygen to hydrogen peroxide, may contribute to disulfide bond formation in a variety of secreted proteins,[30] destroying cellular redox homeostasis. With the accumulation of **2-N3** in mitochondria, the mitochondrial ribosomal protein S11 reduced about 52%. The significant down-regulation of these proteins indicated that **2-N3** had a great influence on transcription, post-translational glycosyl modification, and redox homeostasis in cells.

Besides, some proteins were destroyed in **2-N3**-treated A2780 cells, as no signals were detected by quantitative MS identification. These proteins are listed in Table 2. Among these proteins, the nuclear regulator BRCA1 positively regulated the apoptotic process. Damaged binding proteins included metal

 This journal is © The Royal Society of Chemistry 2019

Published on 18 July 2019. Downloaded by Nottingham Trent University on 8/18/2019 11:29:11 AM.

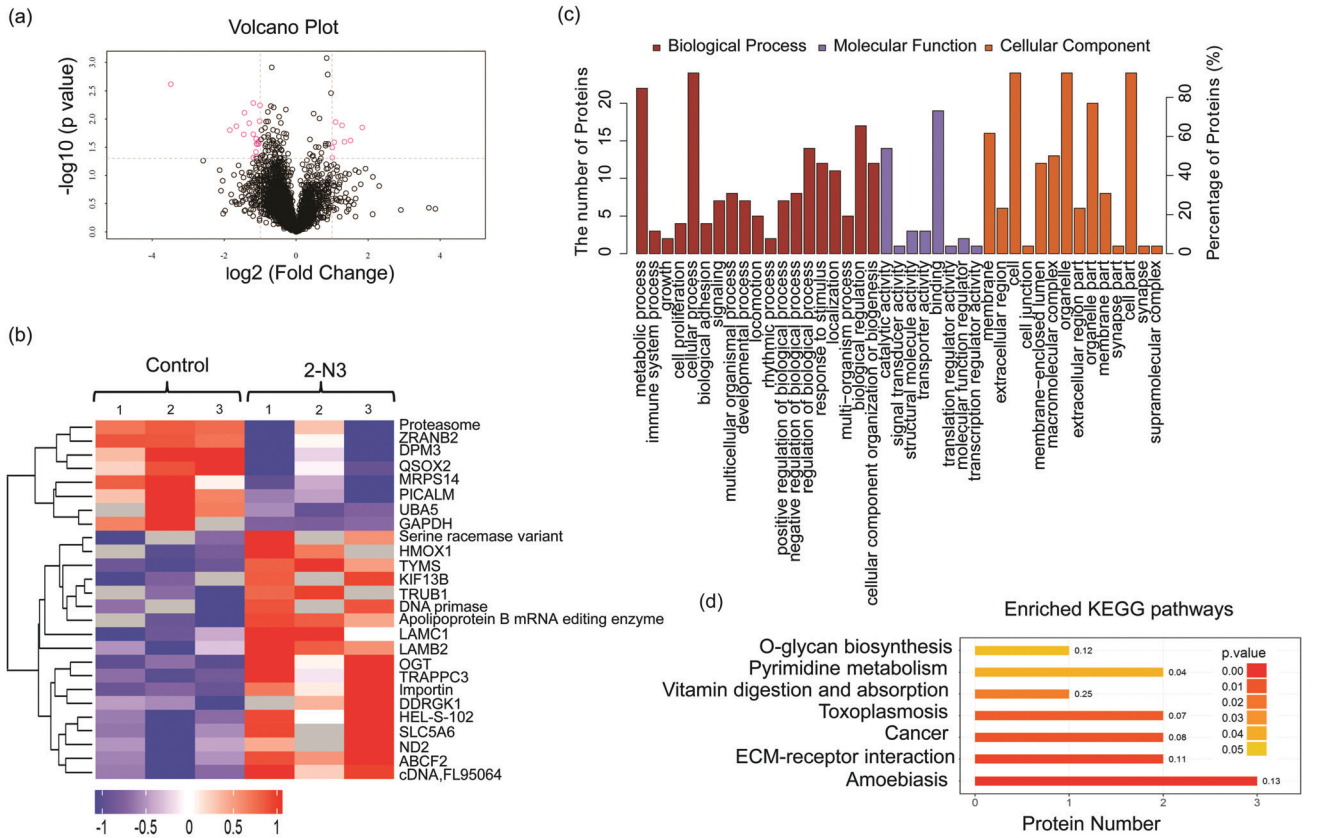

Fig. 4 Proteomic analysis of **2-N3** treated cells. (a) Volcano plot graph of significantly different proteins in **2-N3** treated cells compared with control groups. (b) Heat maps of the 26 most significantly different proteins in **2-N3** treated cells as detected by label-free quantitative analysis ($P < 0.05$). Samples detected were three replications. (c) GO function enrichment analysis of **2-N3** treated cells. GO secondary function annotation (GO Level 2), including the biological process (red), the molecular function (purple) and the cellular component (orange), and the ordinate (right) indicates the difference under each functional classification. The number of expressed proteins; the ordinate (left) indicates the percentage of differentially expressed proteins per functional classification as a percentage of the total differentially expressed protein. (d) KEGG pathway enrichment analysis of **2-N3** treated cells. The ordinate indicates a significantly enriched KEGG pathway, and the abscissa indicates the number of differentially expressed proteins contained in each KEGG pathway. Color gradient represents the *p* value.

ion binding protein RC3H1, ATP binding protein ERCC2, fatty-acyl-CoA binding (lipid binding) protein ACBD5, DNA-binding transcription protein ARNT, zinc ion binding protein CA14, KIF1-binding protein, acidic fibroblast growth factor intracellular-binding protein FIBP and the guanine nucleotide-binding proteins (G proteins) GNG12. Some key enzymes, including cytochrome-*c* oxidase COX1, poly[ADP-ribose] polymerase and nuclear enzymes such as histone H3–K4 methylation ASH2L, DNA repair enzyme TDP2 and nuclear factor of kappa light polypeptide gene enhancer in B-cells 1 (NFKB1) were also disturbed, which may partially be related to the accumulation of **2-N3** in the nucleus. In mitochondria, the mitochondrial BOLA3 protein acts as an assembly factor that facilitates (Fe–S) cluster insertion into a subset of mitochondrial proteins and maintains the integrity of the mitochondrial morphology.[31,32] The mitochondrial ribosomal protein S11 was also destroyed. Deletion of the BOL3 protein and mitochondrial ribosomal protein S11 was likely to cause mitochondrial dysfunction and morphological disorders, associated with morphological damage in mitochondria as previously described (Fig. 2d). Besides, Golgi protein COG3 was also destroyed, which is a transporter from the endoplasmic reticulum to the Golgi.[33] The destruction of these important enzymes related to cellular metabolism, DNA replication and repair, *etc.*, led to the disorder of the entire cellular process.

Conclusions

In summary, we have designed and synthesized a new iridium-hydride complex **2-N3** with both azide and nitrone units. Complex **2-N3** has shown significant antiproliferative activity towards A2780 human ovarian cancer cells. Data suggested that the over-production of ROS induced by complex **2-N3** might contribute to the anticancer activity. Both cellular imaging *via* CuAAC reaction and ICP-MS analysis revealed that complex **2-N3** was scattered in the nucleus and cytoplasm. Further mechanism study by label-free quantitative proteomics analysis indicated that the expression levels of 18 proteins significantly increased and 8 proteins decreased in **2-N3** treated cells. By screening the KEGG pathway database, **2-N3** activated the ECM–receptor interaction pathway by increasing the expression

Published on 18 July 2019. Downloaded by Nottingham Trent University on 8/18/2019 11:29:11 AM.

Table 2 A list of destroyed proteins by **2-N3**

Protein ID	Unique peptides	Coverage (%)	Protein name
Q9UBI6	3	56.9	Guanine nucleotide-binding protein G(I)/G(S)/G(O)
H7C1Z9	3	40.4	Peptidylprolyl isomerase
Q53S33	3	32.7	BolA-like protein 3
Q53FX9	4	29.9	Mitochondrial ribosomal protein S11
A0A087WWF6	8	24.8	DNA polymerase delta
E9PJK1	2	21.8	Tetraspanin
Q9BX67	4	17.4	Junctional adhesion molecule C
Q9UHR4	7	16.8	Brain-specific angiogenesis inhibitor 1-associated protein 2-like protein 1
H0YAA8	2	12.8	Mediator of RNA polymerase II transcription subunit 28
A8K3J4	3	11	Carbonic anhydrase XIV
Q8N4U2	2	11	DHX57 protein
Q6IBU4	2	10.9	SDF2 protein
O95551	3	9.7	Tyrosyl-DNA phosphodiesterase 2
F5H8F7	4	9.6	Set1/Ash2 histone methyltransferase complex subunit ASH2
I6L9E7	3	9.6	ARNT protein
B4DV82	3	8.8	Poly[ADP-ribose] polymerase
A0A024R732	4	8.7	Syntrophin, beta 2
A2VCL3	3	8.7	COG4 protein
E9PSD3	3	8.6	Acidic fibroblast growth factor intracellular-binding protein
A0A059QX78	2	7.6	Cytochrome *c* oxidase subunit 1
A0A1B0GUA3	3	7.1	KIF1-binding protein
Q8TEZ9	3	6.2	SR rich protein
A0A024RDJ4	4	5.7	Nuclear factor of kappa light polypeptide gene enhancer in B-cells 1
B7Z2R7	3	5.7	Acyl-CoA-binding domain-containing protein 5
O94874	4	5.5	E3 UFM1-protein ligase 1
Q3B874	2	4.9	STRN protein
A0A024RDV5	4	4.8	Fibronectin type III domain containing 3A
B3KRK1	2	4.4	Amphoterin-induced protein 2
A0A024R911	2	4.2	Xenotropic and polytropic retrovirus receptor
Q96JB2	2	3.3	Conserved oligomeric Golgi complex subunit 3
A8MX75	2	3.1	General transcription and DNA repair factor IIH helicase subunit XPD
A4D212	5	2.7	DKFZP586J0619 protein
Q53F80	2	2.7	BRCA1 associated RING domain 1 variant
B7ZMB3	2	2.1	RC3H1 protein

of laminin proteins LAMC1 and LAMB2. Analysis of down-regulated proteins suggested an inhibition of DNA transcription, post-translational glycosylation modification, and redox homeostasis by **2-N3**. Finally, the destruction of several important enzymes, related to cellular metabolism and DNA replication and repair, led to the disorder of cellular processes. Our results provided a chemical biology approach employing click chemistry and proteomic analysis in the mechanism study of metallodrugs.

Experimental

Materials and instrumentation

All solvents were of analytical reagent grade and purified according to standard procedures.[34] Chloro(1,5-cyclooctadiene)iridium(I) dimer was purchased from Sinocompound. $AgSbF_6$ was purchased from Alfa Aesar. 4-Chlorobenzaldehyde, 4-(2-pyridinyl)benzaldehyde, *N*-isopropyl-hydroxylamine hydrochloride, 3-picolyl chloride hydrochloride, 3,3-dimethylbut-1-ene, triphenylphosphine, Na_2SO_4 and $NaHCO_3$ were purchased from Adamas. Sodium azide was purchased from Xiya Reagent. All these chemicals were used without further purification.

Human ovarian cancer cells (A2780), human lung cancer cells (H1299), human liver cancer cells (HepG-2), human breast cancer cells (MCF-7), and human normal hepatic cells (L-02) were purchased from the American Type Culture Collection (Manassas, VA). None of the cell lines were listed by the International Cell Line Authentication Committee as cross-contaminated or misidentified (v8.0, 2016). All the cell lines were authenticated by using STR typing and confirmed to be mycoplasma-free by KeyGEN BioTECH Co., Ltd (Nanjing, China). All cells were cultured in 1640 or DMEM (Gibco) containing 10% FBS (Gibco), 100 units per mL penicillin, and 50 units per mL streptomycin at 37 °C in a CO_2 incubator (95% relative humidity, 5% CO_2). All reagents were purchased from Sigma unless otherwise indicated.

Nuclear magnetic resonance (NMR) spectra were acquired on a Bruker 400 MHz AVANCE III for ^1H NMR and ^{13}C NMR at 298 K using deuterated solvents. Chemical shifts (δ, ppm) were reported relative to tetramethylsilane (TMS) as the internal standard and the coupling constants are indicated in hertz (Hz). ESI-MS spectra were recorded on a Mariner System 5304 mass spectrometer. TLC was performed on glass-backed silica gel sheets (silica gel HG/T2354-92 GF254) and visualized under UV light (254 nm). Column chromatography was performed using silica gel (300–400 mesh).

Syntheses of complex 2-N3 and related ligands

Synthesis of 3-(azidomethyl)pyridine (AMP ligand), $IrH_2(PPh_3)_2(C_3H_6O)_2SbF_6$ and alkyne–rhodamine was according to our previous work.[35]

Synthesis of nitrone ligand. A solution of isopropyl hydroxylamine hydrochloride (2 mmol, 250 mg), aldehyde (2 mmol,

 This journal is © The Royal Society of Chemistry 2019

Published on 18 July 2019. Downloaded by Nottingham Trent University on 8/18/2019 11:29:11 AM.

366 mL), Na_2SO_4 (6 mmol, 852 mg), and $NaHCO_3$ (6 mmol, 504 mg) in DCM (15 mL) was heated under reflux in N_2 atmosphere for 48 h. The solids were removed by filtration through Celite, and the solvent was then removed under vacuum. The target product was purified by column chromatography PE/EA (3 : 1, v/v) to yield a white solid.

Syntheses of complex 2-N3. A solution of nitrone ligand (0.55 mmol, 132 mg), $IrH_2(PPh_3)_2(C_3H_6O)_2SbF_6$ (0.5 mmol, 556 mg) and 3,3-dimethylbut-1-ene (2.0 mmol, 242 mg) in 3 mL acetone in a 15 mL Schlenk tube was stirred and heated under reflux for 24 h. The solvent was removed under vacuum, and the residue was washed with diethyl ether or pentane three times. The target products were dried under vacuum to obtain it as a pale yellow solid powder. Then to a 25 mL Schlenk tube was added 0.12 mmol of the yellow solid, 0.60 mmol of 3-(methylazido)pyridine, and 2 mL of anhydrous dichloromethane. After stirring under nitrogen for about 12 h, the mixture was then diluted with diethyl ether and filtered to give a yellow solid **2-N3** (yield = 92%).

X-ray crystallographic study

Diffraction data were collected on an Oxford Diffraction Gemini four-circle system with a Ruby CCD area detector. Using Olex2,[36] the structure was solved with the ShelXT[37] structure solution program using Direct Methods and refined with the ShelXL[38] refinement package using least squares minimization. All the non-hydrogen atoms were refined anisotropically and the hydrogen atoms of the organic molecule were refined in calculated positions, assigned isotropic thermal parameters, and allowed to ride their parent atoms. Crystallographic data (excluding structure factors) for the structures reported in this paper have been deposited with the Cambridge Crystallographic Data Centre with the reference numbers 1514789.† Details of the crystal parameters, data collection and refinement for IrFN were listed in Table S1 (ESI†).

Cytotoxicity assay

A stock solution of the new iridium complexes and cisplatin was first prepared in DMSO and then serially diluted with media to the desired test concentration. *In vitro* cytotoxity assay was performed using a CCK-8 cell proliferation and activity assay kit (KeyGEN BioTECH Co., Ltd, Nanjing, China) according to the supplier's instructions. Briefly, 5000 cells per well were seeded in 96-well plates. The cells were preincubated at 37 °C in a 5% CO_2 humidified atmosphere for 12 h, and the supernatants were removed by suction and washed with PBS twice carefully. Then, 100 μL of media containing different concentrations of complexes and cisplatin were incubated for 48 h, with cisplatin assayed as a positive control. To ensure the reliability of the data, each set contained four parallel hole concentrations. Subsequently, 10 μL CCK-8 was added to each well, and the incubation continued for an additional 3 h. The colour intensity of the medium was measured at 490 nm using a microplate reader (Tecan Infinite M1000 PRO) to calculate the cell viability. According to the calculated inhibition rate and its corresponding complex concentration, the IC_{50} value of the drug concentration corresponding to the inhibition rate at 50% was calculated using ORIGINPRO 8 statistical analysis.

Cellular distribution of complex 2-N3 in cells by ICP-MS

The concentration of A2780 cells in culture flasks was approximately 1×10^6 cells per mL in culture flasks containing DMEM with 10% FBS incubated in a 5% CO_2 and 37 °C incubator for 24 h. After the addition of 5 μM complex **2-N3** and further incubation at 5% CO_2 and 37 °C for 3 h, the medium containing the complex was removed, washed three times with PBS to completely remove residual metal complexes, digested with trypsin, and washed twice with PBS. The cells were collected by centrifugation using the Mitochondria/Nuclei Preparation Kit (KeyGEN BioTECH Co., Ltd, Nanjing, China). Then, the nuclei, mitochondria, and remaining cytoplasm fractions were quantified by ICP-MS analysis.

Cellular ROS detection

We used the fluorescent probe 7-dichlorodihydro-fluoresce indiacetate (DCFH-DA) to study the level of ROS in A2780 cells induced by **2-N3**. A2780 cells were seeded and incubated in 6 well plates for 24 h. Then cells were treated with 5 μM **2-N3** for 3 h and 2 μM Rosup (a reagent that can increase cellular ROS level quickly) as a positive control. Then the medium was removed, 10 μM DCFH-DA was added and kept at 37 °C for 30 min, and then washed three times and finally the cells were collected for flow cytometry detection at 488 nm channel.

Morphological observation of mitochondria

The cells were seeded in a 35 mm glass bottom confocal culture dish and incubated for 24 h. Then the cells were treated with 5 μM **2-N3** for 2 h, with non-treated cells as a control. After washing three times, 200 nM Mito Track Green (KeyGEN BioTECH Co., Ltd, Nanjing, China) was added into the cells, incubated for 45 min. The staining solution was removed and washed three times with PBS until the residual probe was completely removed. The cells were fixed with 4% paraformaldehyde for 20 min, subjected to cell membrane permeation treatment with Triton-X100 for 15 min, and washed twice with PBS. Then the cells were observed using a Fluorescence Microscope ZEISS Axio Observer Z1 and Apotome2 software.

Imaging of 2-N3 *via* Cu(I)-catalysed azide–alkyne cycloaddition reaction

The cells were seeded onto microscope cover slips and treated with **2-N3** (3 μM) for 3 h, with non-treated cells as a control. The cells were then washed with PBS twice, fixed with 4% paraformaldehyde for 20 min, permeabilized with Triton-X100 for 15 min and washed twice with 3% BSA for 10 min. The CuAAC reaction occurred with 0.5 mM $CuSO_4$, 5 mM THPTA, 25 mM sodium ascorbate, 100 mM phosphate buffer and 5 μM alkyne–rhodamine for 2 h at room temperature. The cells were washed with 3% BSA for 5 min, Triton-X100 twice for 10 min, and then the slides were incubated with one drop ProLong Diamond Antifade Reagent with DAPI (Sigma) for 24 h at room temperature. A control group without Cu(I) was prepared following the same

Published on 18 July 2019. Downloaded by Nottingham Trent University on 8/18/2019 11:29:11 AM.

labelling protocol. The cells were observed using a Fluorescence Microscope ZEISS Axio Observer Z1 and Apotome2 software.

Proteomic analysis

Human ovarian cancer A2780 cells were treated with 5 μM complex **2-N3** for 3 h, and cells treated with 0.02% DMSO were used as the control group. One volume of SDT buffer (4% SDS, 100 mM DTT, 150 mM Tris–HCl pH 8.0) was added, and the solution was boiled for 15 min and centrifuged at 14 000*g* for 20 min. Protein digestion (200 μg for each sample) was performed according to the FASP procedure described by Mann *et al.*[39] Briefly, the detergent, DTT and other low-molecular-weight components were removed by using 200 μL of UA buffer (8 M urea, 150 mM Tris–HCl pH 8.0) for repeated ultrafiltration (Microcon units, 30 kD) facilitated by centrifugation. One hundred microlitres of iodoacetamide (0.05 M in UA buffer) was added to block reduced cysteine residues, and the samples were incubated for 20 min in the dark. The filter was washed three times with 100 μL of UA buffer and then twice with 100 μL of 25 mM NH_4HCO_3. Finally, the protein suspension was digested with 3 μg of trypsin (Promega) in 40 μL of 25 mM NH_4HCO_3 overnight at 37 °C, and the resulting peptides were collected as a filtrate. The peptide content was estimated by the UV light spectral density at 280 nm by using an extinction coefficient of 1.1 for 0.1% (g L^{-1}) solution, calculated based on the frequency of tryptophan and tyrosine in vertebrate proteins. Each fraction was injected into a Q Exactive mass spectrometer (Thermo Scientific) for LC-MS/MS analysis. The detection method was positive ion, and the ion scanning range was 300–1800 *m*/*z*. The primary mass spectrometer resolution was 70 000 at 200 *m*/*z* and the AGC (automatic gain control) target was 1e6, the Maximum IT was 50 ms, and the dynamic exclusion time was 60 s. The mass/charge ratio of the polypeptide and polypeptide fragments was collected as follows: 20 fragments were acquired after each full scan, the MS2 Activation Type was HCD, and the Isolation window was 2 *m*/*z*. The rate was 17 500 at 200 *m*/*z*, the normalized collision energy was 30 eV, and the Underfill was 0.1%. All identified proteins were retrieved from the UniProtKB human database (Release 2017_02) in FASTA format. In this study, we used the label-free quantification algorithm for quantification.[40] The GO analysis was carried out with Blast2GO. KEGG pathway annotation on the target protein set was performed using KAAS (KEGG Automatic Annotation Server) software. Protein clustering was performed as follows: the quantitative information of the target protein collection was normalized, and then the cluster 3.0 software was used to classify the two dimensions of the sample and protein expression, and finally the hierarchical clustering heat map was generated using Java Trewview software. All experiments were repeated three times to ensure the reproducibility of the results.

Conflicts of interest

There are no conflicts to declare in this work.

Acknowledgements

Financial support was provided by the National Natural Science Foundation of China (21622103, 21571098, 21671099 and 91753121), Shenzhen Basic Research Program (JCYJ20170413150538897, JCYJ20180508182240106) and the Fundamental Research Funds for the Central Universities (020814380109).

Notes and references

1 K. Wang, C. C. Zhu, Y. F. He, Z. Q. Zhang, W. Zhou, N. Muhammad, Y. Guo, X. Y. Wang and Z. J. Guo, Restraining Cancer Cells by Dual Metabolic Inhibition with a Mitochondrion-Targeted Platinum(ii) Complex, *Angew. Chem., Int. Ed.*, 2019, **58**, 4638–4643.

2 H. Huang, B. Yu, P. Zhang, J. Huang, Y. Chen, G. Gasser, L. Ji and H. Chao, Highly Charged Ruthenium(ii) Polypyridyl Complexes as Lysosome-Localized Photosensitizers for Two-Photon Photodynamic Therapy, *Angew. Chem., Int. Ed.*, 2015, **54**, 14049–14052.

3 Z. Liu, I. Romero-Canelon, B. Qamar, J. M. Hearn, A. Habtemariam, N. P. E. Barry, A. M. Pizarro, G. J. Clarkson and P. J. Sadler, The Potent Oxidant Anticancer Activity of Organoiridium Catalysts, *Angew. Chem., Int. Ed.*, 2014, **53**, 3941–3946.

4 M. A. Scharwitz, I. Ott, R. Gust, A. Kromm and W. S. Sheldrick, Synthesis, cellular uptake and structure-activity relationships for potent cytotoxic trichloridoiridium(iii) polypyridyl complexes, *J. Inorg. Biochem.*, 2008, **102**, 1623–1630.

5 M. Dobroschke, Y. Geldmacher, I. Ott, M. Harlos, L. Kater, L. Wagner, R. Gust, W. S. Sheldrick and A. Prokop, Cytotoxic Rhodium(iii) and Iridium(iii) Polypyridyl Complexes: Structure-Activity Relationships, Antileukemic Activity, and Apoptosis Induction, *ChemMedChem*, 2009, **4**, 177–187.

6 V. Novohradsky, L. Zerzankova, J. Stepankova, A. Kisova, H. Kostrhunova, Z. Liu, P. J. Sadler, J. Kasparkova and V. Brabec, A dual-targeting, apoptosis-inducing organometallic half-sandwich iridium anticancer complex, *Metallomics*, 2014, **6**, 1491–1501.

7 C.-H. Leung, H.-J. Zhong, H. Yang, Z. Cheng, D. S.-H. Chan, V. P.-Y. Ma, R. Abagyan, C.-Y. Wong and D.-L. Ma, A Metal-Based Inhibitor of Tumor Necrosis Factor-alpha, *Angew. Chem., Int. Ed.*, 2012, **51**, 9010–9014.

8 R. C. Bernotas, C. E. Thomas, A. A. Carr, T. R. Nieduzak, G. Adams, D. F. Ohlweiler and D. A. Hay, Synthesis and radical scavenging activity of 3,3-dialkyl-3,4-dihydro isoquinoline 2-oxides, *Bioorg. Med. Chem. Lett.*, 1996, **6**, 1105–1110.

9 R. A. Floyd, R. A. Towner, T. He, K. Hensley and K. R. Maples, Translational research involving oxidative stress and diseases of aging, *Free Radical Biol. Med.*, 2011, **51**, 931–941.

10 D. Nakae, F. Uematsu, H. Kishida, O. Kusuoka, S. Katsuda, M. Yoshida, M. Takahashi, A. Maekawa, A. Denda, Y. Konishi, Y. Kotake and R. A. Floyd, Inhibition of the development of hepatocellular carcinomas by phenyl *N*-*tert*-butyl nitrone in rats fed with a choline-deficient, L-amino acid-defined diet, *Cancer Lett.*, 2004, **206**, 1–13.

 This journal is © The Royal Society of Chemistry 2019

Published on 18 July 2019. Downloaded by Nottingham Trent University on 8/18/2019 11:29:11 AM.

11 R. A. Floyd, H. C. Castro Faria Neto, G. A. Zimmerman, K. Hensley and R. A. Towner, Nitrone-based therapeutics for neurodegenerative diseases: their use alone or in combination with lanthionines, *Free Radical Biol. Med.*, 2013, **62**, 145–156.
12 D. Trachootham, J. Alexandre and P. Huang, Targeting cancer cells by ROS-mediated mechanisms: a radical therapeutic approach?, *Nat. Rev. Drug Discovery*, 2009, **8**, 579–591.
13 X. Song, Y. Qian, R. Ben, X. Lu, H.-L. Zhu, H. Chao and J. Zhao, Activation of C-H Bonds in Nitrones Leads to Iridium Hydrides with Antitumor Activity, *J. Med. Chem.*, 2013, **56**, 6531–6535.
14 B. Rosenberg, L. Vancamp and T. Krigas, Inhibition Of Cell Division In Escherichia Coli by Electrolysis Products From a Platinum Electrode, *Nature*, 1965, **205**, 698–699.
15 F. Arnesano, M. Losacco and G. Natile, An Updated View of Cisplatin Transport, *Eur. J. Inorg. Chem.*, 2013, 2701–2711.
16 E. R. Jamieson and S. J. Lippard, Structure, recognition, and processing of cisplatin-DNA adducts, *Chem. Rev.*, 1999, **99**, 2467–2498.
17 S. Ding, X. Qiao, J. Suryadi, G. S. Marrs, G. L. Kucera and U. Bierbach, Using Fluorescent Post-Labeling To Probe the Subcellular Localization of DNA-Targeted Platinum Anticancer Agents, *Angew. Chem., Int. Ed.*, 2013, **52**, 3350–3354.
18 R. Wirth, J. D. White, A. D. Moghaddam, A. L. Ginzburg, L. N. Zakharov, M. M. Haley and V. J. DeRose, Azide vs Alkyne Functionalization in Pt(ii) Complexes for Post-treatment Click Modification: Solid-State Structure, Fluorescent Labeling, and Cellular Fate, *J. Am. Chem. Soc.*, 2015, **137**, 15169–15175.
19 L. C. C. Lee, J. C. W. Lau, H. W. Liu and K. K. W. Lo, Conferring Phosphorogenic Properties on Iridium(iii)-Based Bioorthogonal Probes through Modification with a Nitrone Unit, *Angew. Chem., Int. Ed.*, 2016, **55**, 1046–1049.
20 V. Pierroz, T. Joshi, A. Leonidova, C. Mari, J. Schur, I. Ott, L. Spiccia, S. Ferrari and G. Gasser, Molecular and Cellular Characterization of the Biological Effects of Ruthenium(II) Complexes Incorporating 2-Pyridyl-2-pyrimidine-4-carboxylic Acid, *J. Am. Chem. Soc.*, 2012, **134**, 20376–20387.
21 J. Maksimoska, L. Feng, K. Harms, C. L. Yi, J. Kissil, R. Marmorstein and E. Meggers, Targeting Large Kinase Active Site with Rigid, Bulky Octahedral Ruthenium Complexes, *J. Am. Chem. Soc.*, 2008, **130**, 15764–15765.
22 A. Wilbuer, D. H. Vlecken, D. J. Schmitz, K. Kraling, K. Harms, C. P. Bagowski and E. Meggers, Iridium complex with antiangiogenic properties, *Angew. Chem., Int. Ed.*, 2010, **49**, 3839–3842.
23 M. V. Babak, S. M. Meier, K. V. M. Huber, J. Reynisson, A. A. Legin, M. A. Jakupec, A. Roller, A. Stukalov, M. Gridling, K. L. Bennett, J. Colinge, W. Berger, P. J. Dyson, G. Superti-Furga, B. K. Keppler and C. G. Hartinger, Target profiling of an antimetastatic RAPTA agent by chemical proteomics: relevance to the mode of action, *Chem. Sci.*, 2015, **6**, 2449–2456.
24 S. M. Meier, D. Kreutz, L. Winter, M. H. M. Klose, K. Cseh, T. Weiss, A. Bileck, B. Alte, J. C. Mader, S. Jana, A. Chatterjee, A. Bhattacharyya, M. Hejl, M. A. Jakupec, P. Heffeter, W. Berger, C. G. Hartinger, B. K. Keppler, G. Wiche and C. Gerner, An Organoruthenium Anticancer Agent Shows Unexpected Target Selectivity For Plectin, *Angew. Chem., Int. Ed.*, 2017, **56**, 8267–8271.
25 M. A. Eckert, F. Coscia, A. Chryplewicz, J. W. Chang, K. M. Hernandez, S. Pan, S. M. Tienda, D. A. Nahotko, G. Li, I. Blazenovic, R. R. Lastra, M. Curtis, S. D. Yamada, R. Perets, S. M. McGregor, J. Andrade, O. Fiehn, R. E. Moellering, M. Mann and E. Lengyel, Proteomics reveals NNMT as a master metabolic regulator of cancer-associated fibroblasts, *Nature*, 2019, **569**, 723–728.
26 S. Gotz, J. M. Garcia-Gomez, J. Terol, T. D. Williams, S. H. Nagaraj, M. J. Nueda, M. Robles, M. Talon, J. Dopazo and A. Conesa, High-throughput functional annotation and data mining with the Blast2GO suite, *Nucleic Acids Res.*, 2008, **36**, 3420–3435.
27 M. Kanehisa, S. Goto, Y. Sato, M. Furumichi and M. Tanabe, KEGG for integration and interpretation of large-scale molecular data sets, *Nucleic Acids Res.*, 2012, **40**, D109–D114.
28 D. K. Banerjee, Z. Zhang, K. Baksi and J. E. Serrano-Negron, Dolichol phosphate mannose synthase: a glycosyltransferase with unity in molecular diversities, *Glycoconjugate J.*, 2017, **34**, 467–479.
29 D. J. Adams, L. van der Weyden, A. Mayeda, S. Stamm, B. J. Morris and J. E. J. Rasko, ZNF265 – a novel spliceosomal protein able to induce alternative splicing, *J. Cell Biol.*, 2001, **154**, 25–32.
30 I. Wittke, R. Wiedemeyer, A. Pillmann, L. Savelyeva, F. Westermann and M. Schwab, Neuroblastoma-derived sulfhydryl oxidase, a new member of the sulfhydryl oxidase/Quiescin6 family, regulates sensitization to interferon gamma-induced cell death in human neuroblastoma cells, *Cancer Res.*, 2003, **63**, 7742–7752.
31 M. A. Uzarska, V. Nasta, B. D. Weiler, F. Spantgar, S. Ciofi-Baffoni, M. R. Saviello, L. Gonnelli, U. Muhlenhoff, L. Banci and R. Lill, Mitochondrial Bol1 and Bol3 function as assembly factors for specific iron-sulfur proteins, *eLife*, 2016, **5**, 16673.
32 P. Willems, B. F. J. Wanschers, J. Esseling, R. Szklarczyk, U. Kudla, I. Duarte, M. Forkink, M. Nooteboom, H. Swarts, J. Gloerich, L. Nijtmans, W. Koopman and M. A. Huynen, BOLA1 Is an Aerobic Protein That Prevents Mitochondrial Morphology Changes Induced by Glutathione Depletion, *Antioxid. Redox Signaling*, 2013, **18**, 129–138.
33 E. Loh and W. J. Hong, Sec34 is implicated in traffic from the endoplasmic reticulum to the Golgi and exists in a complex with GTC-90 and ldlBp, *J. Biol. Chem.*, 2002, **277**, 21955–21961.
34 P. M. Schwab, C. Moosmann, K. Dopf and H. J. Eisler, Oxide mediated spectral shifting in aluminum resonant optical antennas, *Opt. Express*, 2015, **23**, 26533–26543.
35 X. Wang, M. Zhu, F. Gao, W. Wei, Y. Qian, H. K. Liu and J. Zhao, Imaging of a clickable anticancer iridium catalyst, *J. Inorg. Biochem.*, 2018, **180**, 179–185.
36 O. V. Dolomanov, L. J. Bourhis, R. J. Gildea, J. A. K. Howard and H. Puschmann, OLEX2: a complete structure solution,

refinement and analysis program, *J. Appl. Crystallogr.*, 2009, **42**, 339–341.

37 G. M. Sheldrick, SHELXT-integrated space-group and crystal-structure determination, *Acta Crystallogr., Sect. A: Found. Adv.*, 2015, **71**, 3–8.

38 G. M. Sheldrick, Crystal structure refinement with SHELXL, *Acta Crystallogr., Sect. C: Struct. Chem.*, 2015, **71**, 3–8.

39 J. R. Wiśniewski, A. Zougman, N. Nagaraj and M. Mann, Universal sample preparation method for proteome analysis, *Nat. Methods*, 2009, **6**, 359–362.

40 J. Cox, M. Y. Hein, C. A. Luber, I. Paron, N. Nagaraj and M. Mann, Accurate proteome-wide label-free quantification by delayed normalization and maximal peptide ratio extraction, termed MaxLFQ, *Mol. Cell. Proteomics*, 2014, **13**, 2513–2526.

Published on 18 July 2019. Downloaded by Nottingham Trent University on 8/18/2019 11:29:11 AM.

This journal is © The Royal Society of Chemistry 2019